

Structural relaxations around Ti, Cr and Fe impurities in α -Al₂O₃ probed by x-ray absorption near edge structure combined with first-principles calculations

Emilie Gaudry, Delphine Cabaret, Philippe Saintavitt, Christian Brouder, Francesco Mauri,
Laboratoire de Minéralogie-Cristallographie
UMR CNRS 7590, Université Pierre et Marie Curie,
case 115, 4 place Jussieu
F-75252 Paris Cedex 05, France

José Goulon, Andrei Rogalev
European Synchrotron Radiation Facility
BP 220, F-38043 Grenoble Cedex, France
(Dated: January 12, 2005)

We determine the structural relaxations around paramagnetic impurities (Ti, Cr, Fe) in corundum (α -Al₂O₃), by combining x-ray absorption near edge structure (XANES) experiments and *ab initio* calculations. The structural relaxations are found to be very local. We then show that XANES is sensitive to small variations in interatomic distances within the coordination shell of the absorbing atom. The experiments were carried out on single crystals of ruby and sapphires. Linear dichroic signals are essential to characterize the geometry of the impurity site. The calculations were performed within a self-consistent “non muffin-tin” framework, that uses pseudopotentials, plane-wave basis set, and the continued fraction for the absorption cross section.

PACS numbers: 61.72.-y, 78.70.Dm, 71.15.Mb, 61.66.-f, 85.40.Ry

Keywords: XANES, K edge, *ab initio*, pseudopotentials, ruby, sapphires, impurities, structural relaxation, angular dependence

I. INTRODUCTION

The presence of impurities in a crystal can influence its mechanical, magnetic, semiconducting, superconducting, dielectric, spectroscopic and transport properties. To cite just a few specific examples, impurities can improve the voltage holdoff capability of insulating materials¹, they are critical for the optical properties of most laser materials and gemstones, and they turned out to be the secret of ancient Damascus steel blades.²

Still, the physics of impurity systems is not well developed. The local crystallographic structure around impurities is unknown in most cases, although it is an essential piece of information to understand their influence on the physical properties of the host and to carry out *ab initio* simulations of these materials. This situation is due to the experimental and theoretical difficulties that are met to obtain microscopic information on impurity systems. From the theoretical point of view, quantum calculations of impurity systems require the use of large supercells that have long not been computationally manageable. From the experimental point of view, impurity systems can only be measured with methods which can selectively probe certain atomic species. Among such methods, many of them, such as electronic paramagnetic resonance, give only indirect information on the position and nature of the atoms surrounding the impurity. Due to the advent of third-generation synchrotron radiation facilities, x-ray absorption spectroscopy (XAS) is now able to investigate impurities in solids.

The extended x-ray absorption fine structure (EXAFS) region of a XAS spectrum provides quantitative

information about the short range organization around the absorbing atom (coordination number, interatomic distances). The x-ray absorption near-edge structure (XANES) region usually gives qualitative information about the atomic arrangement up to the medium range order. XANES is sensitive to the electronic structure (bonding) and probes the empty states of solids. In the case of dilute elements in single crystals, especially at the *K* edge of *3d* transition elements, collecting EXAFS spectra with a good signal-to-noise ratio is a difficult task, because the intensity of diffraction peaks becomes much larger than the EXAFS signal. Taking the example of impurities in corundum α -Al₂O₃,³ good EXAFS spectra could be collected for 10000 wt.ppm Cr³⁺ impurities, but the usable energy range obtained for 1500 wt.ppm Fe³⁺ impurities was already quite limited, and the concentration of coloring impurities is often an order of magnitude lower than this. In such cases, XANES becomes a practice and precious technique to get information about the local structure of the absorbing atom.⁴ However, the analysis of the experimental XANES data is not straightforward because of the photoelectron multiple-scattering processes that occur in the near-edge region. *Ab initio* XANES simulations are then required to relate the experimental spectral features to the local geometry around the absorbing atom.

Recently, an efficient first-principle approach based on plane-wave pseudopotential formalism has been developed to calculate *K*-edge XANES spectra.⁵ Here we apply this method to the *K*-edge of substitutional paramagnetic impurities in aluminum oxide. More precisely, we investigate the structural modifications of the corundum

crystal structure induced by the presence of substitutional Ti^{3+} , Cr^{3+} or Fe^{3+} . This system is chosen because corundum containing transition metal impurities is important for laser applications and as gemstones. Colorless corundum ($\alpha\text{-Al}_2\text{O}_3$) becomes red ruby, pink sapphire, or yellow sapphire when a small amount of Cr^{3+} , Ti^{3+} , or Fe^{3+} ions substitute for Al^{3+} ions, respectively.^{6,7} The color of blue sapphire is due to the presence of (Fe-Ti) pairs in $\alpha\text{-Al}_2\text{O}_3$.

For this investigation, polarized XANES spectra are measured and calculated. Corundum belongs to the trigonal Bravais lattice, the optical axis being parallel to the [111] direction of the trigonal unit cell (i.e. to the c -axis of the hexagonal cell). Corundum is then a dichroic compound in the electric dipole approximation. The dichroic signal is a direct signature of the departure of the impurity site from octahedral symmetry.³ XANES calculations are performed from structural models resulting from *ab initio* energy minimization calculations. The agreement of our experimental and theoretical spectra demonstrates that precise structural information can be extracted from the angular-dependent XANES spectra, provided the electronic potential is accurately modelled.

II. EXPERIMENTS

A. Crystallographic structure of $\alpha\text{-Al}_2\text{O}_3$ and samples description

Corundum ($\alpha\text{-Al}_2\text{O}_3$) belongs to the $R\bar{3}c$ (D_{3d}^6) space group.⁸ The trigonal unit cell contains two Al_2O_3 formula units. The atomic environment of aluminum is illustrated in Fig. 1. The atomic site of aluminum is a distorted octahedron with a 3 (C_3) local point symmetry. The AlO_6 octahedron is characterized by two different Al-O interatomic distances. If we consider that the absorbing atom is denoted by Al in Fig. 1, the nearest three oxygen atoms are labeled O_1 in Fig. 1. The farther three oxygen atoms, labeled O_2 , form a face shared by two octahedra along the three-fold symmetry axis. Beyond the coordination shell of aluminum, the next two neighbors are aluminum atoms, labeled Al_1 and Al_2 in Fig. 1, and are relative to face-shared octahedra and edge-shared octahedra, respectively.

Three synthetic single crystals of doped $\alpha\text{-Al}_2\text{O}_3$ (obtained by the Verneuil process) are used for this study: a red ruby ($\alpha\text{-Al}_2\text{O}_3\text{:Cr}^{3+}$), a blue sapphire ($\alpha\text{-Al}_2\text{O}_3\text{:Fe-Ti}$) and a pink sapphire ($\alpha\text{-Al}_2\text{O}_3\text{:Ti}^{3+}$). The impurity concentration in each sample is given in table I. They are measured with the Cameca Microbeam electron microprobe at the CAMPARIS analytical facility of Paris. A 30 kV acceleration with a 15 nA beam current, defocused to $10\mu\text{m}$, is used. X-ray intensities are corrected for dead-time, background, and matrix effects using the Cameca ZAF routine. The standards used are $\alpha\text{-Al}_2\text{O}_3$, $\alpha\text{-Cr}_2\text{O}_3$, $\alpha\text{-Fe}_2\text{O}_3$ and TiO_2 . The blue sapphire sample is chosen to represent the model compound of iron impurity

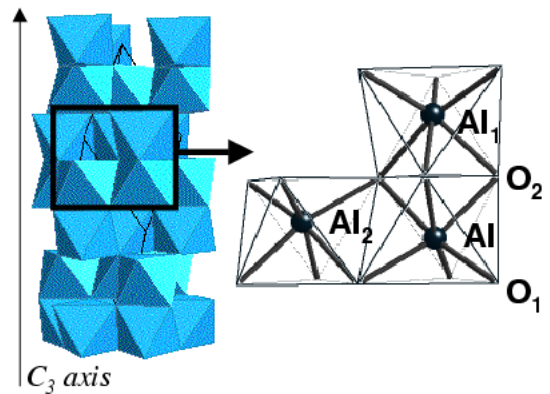


FIG. 1: Aluminum atomic site in corundum. Left: the corundum structure is represented as a stacking of AlO_6 octahedra (the trigonal cell and the three-fold symmetry axis are indicated). Right: zoom of the black-framed region of the left panel. The aluminum site with its O_1 , O_2 , Al_1 and Al_2 first four neighbors are indicated.

in corundum ($\alpha\text{-Al}_2\text{O}_3\text{:Fe}^{3+}$). It is indeed preferred to a yellow sapphire sample, that only contains iron impurities, because synthetic yellow sapphires are known to be inhomogeneous.⁹ Consequently, in this study, we assume that the low concentration of titanium (750 wt.ppm) compared to that of iron (1500 wt.ppm) does not affect the site relaxation around iron.

TABLE I: Impurity concentration (in wt.ppm) in the three doped $\alpha\text{-Al}_2\text{O}_3$ samples.

Samples	Cr (wt.ppm)	Fe (wt.ppm)	Ti (wt.ppm)
Red ruby	10000 (± 1000)	-	-
Blue sapphire	-	1500 (± 50)	750 (± 30)
Pink sapphire	-	-	540 (± 30)

The samples are cylindrically shaped: 15 mm diameter and 3 mm thickness for the ruby sample, and 5 mm diameter and 1 mm thickness for the sapphire samples. They are cut so that the optical axis is in the plane of the disk surface, and the $[10\bar{1}]$ direction of the trigonal cell is orthogonal to the disk surface.

B. X-ray absorption measurements

X-ray absorption measurements are carried out at the European Synchrotron Radiation Facility (ESRF) on the ID12 beam line, which is dedicated to polarization dependent spectroscopies.^{10,11} The monochromatic x-ray beam is obtained through a double $\text{Si}(111)$ crystal monochromator, with a resolution $\Delta E/E \simeq 10^{-4}$. The oriented samples are placed on a rotating holder with the normal of the disk surface parallel to the x-ray wave vector and to the rotation axis. The fluorescence intensity is measured by eight detectors symmetrically set around the

x-ray beam.

XANES spectra are recorded for several angles θ between the optical axis of the sample and the x-ray polarization vector. We note σ_{\parallel} and σ_{\perp} the absorption cross section obtained with $\theta = 0^{\circ}$ and $\theta = 90^{\circ}$, respectively. In the electric dipole approximation, the isotropic signal is given by $(\sigma_{\parallel} + 2\sigma_{\perp})/3$, and the dichroic signal is given by the difference $\sigma_{\parallel} - \sigma_{\perp}$. The measurement of x-ray absorption spectra of impurities in crystals is impeded by the presence of large diffraction peaks. In order to decrease the intensity of diffraction peaks and elastic scattering, V and Mn filters (50 μm width) are used for the Cr K edge in ruby and the Fe K edge in blue sapphire, respectively. By so doing, the spectra recorded for the two angles $\theta = 0^{\circ}$ and $\theta = 90^{\circ}$ are not affected by diffraction peaks. On the contrary, no filter is available for the Ti K edge and the absorption was measured for 100 angles θ from 0 to 360° . The σ_{\parallel} and σ_{\perp} spectra are reconstructed from this amount of data by using a Fourier decomposition to remove the contribution of diffraction peaks to the spectra.

C. Calculation methods

The starting point of any XANES *ab initio* calculation is a structural model. Two structural models are considered for each compound. The first one, called *non-relaxed* model, corresponds to the substitution of one aluminum atom by one impurity Ti, Cr or Fe in the $\alpha\text{-Al}_2\text{O}_3$, without relaxing its structure. The second one, called *relaxed* model, is the result of *ab initio* energy minimization calculation carried out on the *non-relaxed* model. This calculation is performed using Car-Parrinello molecular dynamics with simulated annealing¹² as implemented in the CPMD code.¹³ The XANES calculations are then carried out within the scheme of the PARATEC code,¹⁴ using the formalism described in Ref.⁵ Both codes are based on the density functional theory (DFT) within the spin polarized local density approximation (LSDA), and use plane-wave basis set and norm-conserving Troullier-Martins pseudopotentials¹⁵ in the Kleinman-Bylander form.¹⁶ In the following, we give all the parameters used in both kinds of calculation.

1. Structural model construction

The structural models are constructed from the lattice parameters and atomic positions resulting from a previous *ab initio* calculation, performed by Duan *et al.*^{17,18} in $\alpha\text{-Al}_2\text{O}_3$. In Ref.¹⁷, the trigonal unit cell parameters are $a_R = 5.11 \text{ \AA}$ and $\alpha = 55.41^{\circ}$, the aluminum atoms are in 4 c symmetry sites¹⁹ with $x = 0.352$ and the oxygen atoms are in 6 e symmetry sites¹⁹ with $x = 0.555$. We verify by using CPMD that this corundum optimized structure obtained by Duan *et al.* corresponds to atomic forces less than $2 \cdot 10^{-3} \text{ Ry/\AA}$. Since we use periodic bound-

ary conditions, we consider $2 \times 2 \times 2$ supercells. The supercells contain 80 atoms: 48 oxygen atoms, 31 aluminum atoms and 1 transition metal atom (Ti, Cr or Fe) in substitution for aluminum. With such large supercells, the interaction between two impurities (belonging to two neighboring cells) is negligible. These supercells define the *non-relaxed* models mentioned above. The *relaxed* models are obtained by minimization of the energy of the *non-relaxed* supercells. All atoms are allowed to relax, while the lattice constants are fixed. The impurities considered in this study are known to be in a high-spin state,²⁰ therefore the spin multiplet imposed on the trivalent impurities are $S=\frac{1}{2}$ for Ti^{3+} ($[\text{Ar}]4s^03d^1$), $S=\frac{3}{2}$ for Cr^{3+} ($[\text{Ar}]4s^03d^3$), and $S=\frac{5}{2}$ for Fe^{3+} ($[\text{Ar}]4s^03d^5$). The parametrization of the norm-conserving Troulliers-Martins pseudopotentials is given in Table II. The wave functions and the charge density were expanded in plane waves with cutoff of 80 Ry and 320 Ry, respectively. Since the supercell is rather large, and since the systems are insulating materials, the Brillouin zone is only sampled at the Γ point.

TABLE II: Parametrization used for the generation of the pseudopotentials. The core radii of the valence states are indicated between parenthesis in \AA .

atom	Al	O	Ti	Cr	Fe
valence states	$3s$ (1.06)	$2s$ (0.77)	$3s$ (0.58)	$3s$ (0.53)	$3s$ (0.48)
	$3p$ (1.06)	$2p$ (0.77)	$3p$ (0.90)	$3p$ (0.79)	$3p$ (0.90)
	$3d$ (1.06)		$3d$ (0.90)	$3d$ (0.79)	$3d$ (0.90)
local part	d	p	d	d	d

2. XANES calculations

The method used for XANES calculations has been already described in Ref.^{5,21} Therefore its main aspects are recalled here. The method uses periodic boundary conditions, plane-wave basis-set, pseudopotentials and reconstructs all-electron wave functions within the projector augmented wave (PAW) framework.²² In order to allow the treatment of large supercells (hundreds of atoms), the scheme uses a recursion method to construct a Lanczos basis and then compute the cross section as a continued fraction,^{23,24} in the electric dipole and quadrupole approximations.²⁵ Electric quadrupole transitions are relevant for the pre-edge region, in particular at the K -edge of transition metals. The absorption cross section is calculated beyond the ‘‘muffin-tin’’ approximation, that is known to limit the applications of the multiple scattering theory traditionally used for XANES simulations.^{26,27,28}

XANES spectra are computed at the transition metal K edge for both *relaxed* and *non-relaxed* models of the three compounds, using the 80-atom supercells described in the previous subsection. For the pseudopotentials construction, we again use the parametrization given in Ta-

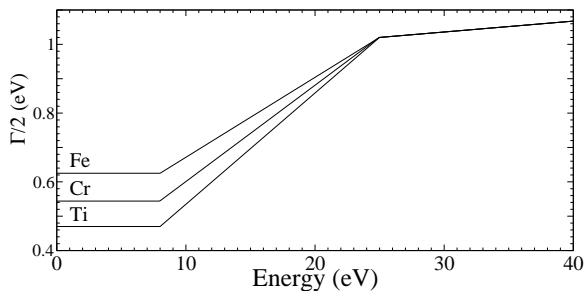


FIG. 2: Energy dependence of the γ parameters used for the convolution of the XANES spectra at the Ti, Cr and Fe K edges in doped α - Al_2O_3 . The zero in the energy scale refers to the highest occupied level in the corresponding structure.

ble II. In order to take into account the core-hole effects in the calculations, the Ti, Cr and Fe pseudopotentials are generated with only one $1s$ electron. The spin multiplet degeneracy is set by imposing the number of up and down states given by the CPMD code. Convergence of the XANES theoretical spectra is reached for the following set of parameters: a 64 Ry energy cutoff and one \mathbf{k} -point for the self-consistent spin-polarized charge density calculation, and 32 \mathbf{k} -points²⁹ for the absorption cross section calculation. An energy dependent broadening parameter γ is used in the continued fraction (see Ref.^{5,21}) in order to account for the two main photoelectron damping modes.³⁰ This width γ corresponds through the time-energy uncertainty relations to a lifetime of the photoelectron. At low energy, the lifetime of the photoelectron is only limited by the core-hole lifetime within the plasmon pole approximation. The parameter γ was then set to a constant, which corresponds to K level full width at half maximum given by Krause and Oliver.³¹ At higher energy, the kinetic energy of the photoelectron is great enough so that it can interact with the electron gas of the system. Its amplitude is damped, provoking a sharp decrease in the lifetime. Therefore the γ parameter was set to rapidly increase, and then to have a smooth linear behaviour. The γ energy-dependent parameters used in this study are displayed in Fig. 2.

III. RESULTS AND DISCUSSION

This section is organized as follows. First, we present the results of the structural relaxation around the substitutional Ti^{3+} , Cr^{3+} and Fe^{3+} ions in α - Al_2O_3 (Sec.III A). Second, we discuss the influence of the core-hole effects in the case of the Cr K -edge in ruby (Sec.III B). Third, we confront with experiments the calculated spectra obtained with both *relaxed* and *non-relaxed* models (Sec.III C).

A. Structural model analysis

The *relaxed* models of α - $\text{Al}_2\text{O}_3:\text{Cr}^{3+}$ and α - $\text{Al}_2\text{O}_3:\text{Fe}^{3+}$ are already described and discussed in a previous work.³ However, in order to compare with the *relaxed* model of α - $\text{Al}_2\text{O}_3:\text{Ti}^{3+}$, most of the results of Ref.³ are recalled here.

The analysis of the relaxation can only be done by careful comparison of the *relaxed* and *non-relaxed* supercells. This is achieved by comparing clusters that are built from the supercells using the method detailed in Ref.³ These clusters are centered on the impurity and contain 66 atoms (5.2 \AA radius). In order to avoid the influence of the impurity displacement in the *relaxed* model, we define the mass center Ω of each cluster by calculating $\vec{O}\Omega = \frac{1}{\sum_i m_i} \sum_i m_i \vec{O}\vec{M}_i$, where O is the impurity position, M_i refers to all the atoms within a given cluster except the impurity and m_i is the mass of the atom i . For each atom i around the impurity, we evaluate the norm of the displacement vector, $|\vec{V}_i|$,

$$|\vec{V}_i|^2 = (X_{relaxed}^i - X_{non-relaxed}^i)^2 + (Y_{relaxed}^i - Y_{non-relaxed}^i)^2 + (Z_{relaxed}^i - Z_{non-relaxed}^i)^2,$$

where $(X_{non-relaxed}^i, Y_{non-relaxed}^i, Z_{non-relaxed}^i)$ and $(X_{relaxed}^i, Y_{relaxed}^i, Z_{relaxed}^i)$ are the cartesian coordinates of $\Omega\vec{M}_i$ vector in the *non-relaxed* and *relaxed* clusters, respectively. The angular relaxation was also determined. It was defined by the quantity $\delta\theta = \theta_{non-relaxed} - \theta_{relaxed}$, where $\theta_{relaxed}$ and $\theta_{non-relaxed}$ are the angles between the $\Omega\vec{M}_i$ directions and the C_3 axis in the *relaxed* and *non-relaxed* clusters, respectively. The comparison of the *relaxed* and *non-relaxed* clusters leads to the following conclusions.

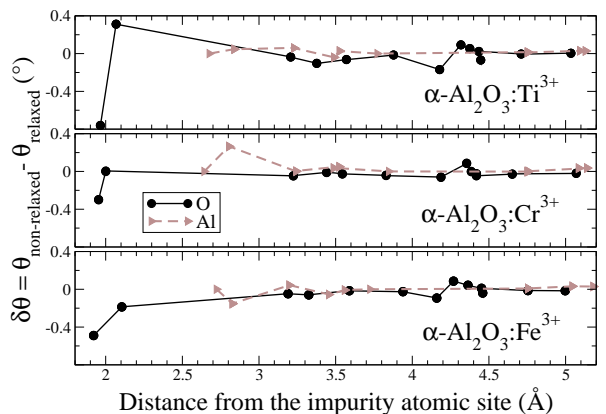


FIG. 3: Angular relaxation around the paramagnetic impurities in doped α - Al_2O_3 : $\delta\theta$ angle (see text for explanation) as a function of distance from the impurity in the *relaxed* model.

First, the impurity site symmetry is conserved: the Ti, Cr and Fe atoms are still in a C_3 point symmetry site, characterized by two kinds of M-O_1 and M-O_2 distances

TABLE III: M-O and M-Al bond lengths in $\alpha\text{-Al}_2\text{O}_3\text{:M}^{3+}$ (M=Ti, Cr, Fe) issued from the energy minimization calculations presented in Sec.III A. These bond lengths are compared with the experimental and calculated Al-O and Al-Al interatomic distances in $\alpha\text{-Al}_2\text{O}_3$ and to the M-O and M-M distances in $\alpha\text{-M}_2\text{O}_3$. It is worth noting that the distances indicated for $\alpha\text{-Al}_2\text{O}_3$ relative to Ref.¹⁸ are the M-O and M-Al distances in the *non-relaxed* models.

Compound	Interatomic distances (in Å)			
	cation-oxygen		cation-cation	
$\alpha\text{-Al}_2\text{O}_3$ (exp. ⁸)	$d_{\text{Al-O}_1} = 1.86$	$d_{\text{Al-O}_2} = 1.97$	$d_{\text{Al-Al}_1} = 2.65$	$d_{\text{Al-Al}_2} = 2.79$
$\alpha\text{-Al}_2\text{O}_3$ (calc. ¹⁸)	$d_{\text{Al-O}_1} = 1.84$	$d_{\text{Al-O}_2} = 1.95$	$d_{\text{Al-Al}_1} = 2.62$	$d_{\text{Al-Al}_2} = 2.77$
$\alpha\text{-Al}_2\text{O}_3\text{:Ti}^{3+}$ (this calc.)	$d_{\text{Ti-O}_1} = 1.97$	$d_{\text{Ti-O}_2} = 2.07$	$d_{\text{Ti-Al}_1} = 2.72$	$d_{\text{Ti-Al}_2} = 2.83$
$\alpha\text{-Al}_2\text{O}_3\text{:Cr}^{3+}$ (calc. ³)	$d_{\text{Cr-O}_1} = 1.95$	$d_{\text{Cr-O}_2} = 2.00$	$d_{\text{Cr-Al}_1} = 2.64$	$d_{\text{Cr-Al}_2} = 2.80$
$\alpha\text{-Al}_2\text{O}_3\text{:Fe}^{3+}$ (calc. ³)	$d_{\text{Fe-O}_1} = 1.92$	$d_{\text{Fe-O}_2} = 2.10$	$d_{\text{Fe-Al}_1} = 2.72$	$d_{\text{Fe-Al}_2} = 2.83$
$\alpha\text{-Ti}_2\text{O}_3$ (exp. ⁸)	$d_{\text{Ti-O}_1} = 2.01$	$d_{\text{Ti-O}_2} = 2.08$	$d_{\text{Ti-Ti}_1} = 2.59$	$d_{\text{Ti-Ti}_2} = 2.99$
$\alpha\text{-Cr}_2\text{O}_3$ (exp. ⁴⁸)	$d_{\text{Cr-O}_1} = 1.96$	$d_{\text{Cr-O}_2} = 2.01$	$d_{\text{Cr-Cr}_1} = 2.65$	$d_{\text{Cr-Cr}_2} = 2.88$
$\alpha\text{-Fe}_2\text{O}_3$ (exp. ⁴⁸)	$d_{\text{Fe-O}_1} = 1.94$	$d_{\text{Fe-O}_2} = 2.11$	$d_{\text{Fe-Fe}_1} = 2.90$	$d_{\text{Fe-Fe}_2} = 2.97$

(M = Ti, Cr or Fe). The angular relaxation is found to be very small (i.e. less than 0.8 degrees). This is illustrated in Fig. 3, which gives $\delta\theta$ as a function of the distance between the impurity and its neighboring atoms in the *relaxed* clusters.

Second, a displacement of the impurity from the initial aluminum site is observed in the three *relaxed* models. This displacement occurs along the C_3 axis, but its absolute value depends on the impurity. Chromium is displaced by 0.03 Å towards Al_1 atom, titanium is displaced by again 0.03 Å but in the opposite direction, and iron is further moved (0.09 Å towards Al_1 atom). The small displacement of chromium is in agreement with various experimental studies of the literature.^{32,33,34,35,36} The result for iron is consistent with an analysis of electronic paramagnetic resonance (EPR) experiments, that gives a displacement of 0.04 ± 0.02 Å.³⁷

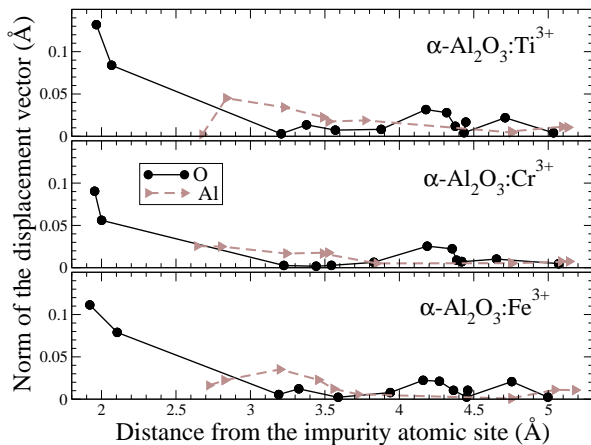


FIG. 4: Radial relaxation around the paramagnetic impurities in doped $\alpha\text{-Al}_2\text{O}_3$: norm of atomic displacement vectors (oxygen atoms in solid line with circles and aluminum atoms in dashed line with triangles) as a function of distance from the impurity in the *relaxed* model.

Third, an increase of distances within the coordination shell of the impurity is observed. This result is

expected since the ionic radii of Ti, Cr and Fe in octahedral site³⁸ ($r_{\text{Ti}^{3+}} = 0.670$ Å, $r_{\text{Cr}^{3+}} = 0.615$ Å and $r_{\text{Fe}^{3+}} = 0.645$ Å) are all greater than the ionic radius of aluminum ($r_{\text{Al}^{3+}} = 0.535$ Å). The calculated M-O₁ and M-O₂ bond lengths in doped $\alpha\text{-Al}_2\text{O}_3$ were found to be close to M-O₁ and M-O₂ bond lengths in the corresponding metal oxides, $\alpha\text{-M}_2\text{O}_3$ ($\alpha\text{-Ti}_2\text{O}_3$, $\alpha\text{-Cr}_2\text{O}_3$ and $\alpha\text{-Fe}_2\text{O}_3$). On the contrary, the distances M-Al₁ and M-Al₂ were less affected by the relaxation process: they are closer to Al-Al₁ and Al-Al₂ bond lengths in corundum than the M-M₁ and M-M₂ distances in the corresponding oxides $\alpha\text{-M}_2\text{O}_3$. Tab.III gathers the M-O₁, M-O₂, M-Al₁ and M-Al₂ distances in $\alpha\text{-Al}_2\text{O}_3\text{:M}^{3+}$ deduced from the calculation, and compares them with the corresponding distances in $\alpha\text{-Al}_2\text{O}_3$, $\alpha\text{-Ti}_2\text{O}_3$, $\alpha\text{-Cr}_2\text{O}_3$ and $\alpha\text{-Fe}_2\text{O}_3$, resulting from x-ray diffraction experiments. One can remark in Tab. III that the Ti-O₁ and Ti-O₂ bond lengths in $\alpha\text{-Al}_2\text{O}_3\text{:Ti}^{3+}$ (1.97 Å and 2.07 Å) are quite similar to those in $\alpha\text{-Ti}_2\text{O}_3$ (2.01 Å and 2.07 Å). Besides, the Ti-Al₁ and Ti-Al₂ distances in $\alpha\text{-Al}_2\text{O}_3\text{:Ti}^{3+}$ (2.72 Å and 2.83 Å) are closer to the Al-Al₁ and Al-Al₂ distances in corundum (2.65 Å and 2.79 Å) than to the Ti-Ti₁ and Ti-Ti₂ distances in $\alpha\text{-Ti}_2\text{O}_3$ (2.59 Å and 2.99 Å). One can notice that the experimental distances Cr-Cr₁ in $\alpha\text{-Cr}_2\text{O}_3$ and Al-Al₁ in $\alpha\text{-Al}_2\text{O}_3$ are both equal to 2.64 Å. Thus one expects that Cr-Al₁ distance in ruby ($\alpha\text{-Al}_2\text{O}_3\text{:Cr}^{3+}$) should be around 2.64 Å. The calculated distances of $\alpha\text{-Al}_2\text{O}_3\text{:Cr}^{3+}$ are slightly larger (+0.015 Å) than those determined from EXAFS measurements on powder samples,³⁶ and in good agreement (+0.005 Å) with EXAFS measurements performed and on the same single crystal as the one used in the present study.³ They are also consistent with data extracted from optical spectroscopy.³⁹ For $\alpha\text{-Al}_2\text{O}_3\text{:Fe}^{3+}$, the calculated distances are in agreement with EXAFS experiments³ and with EPR results.³⁷

Finally, the M-O and M-Al distances deduced from the *ab initio* relaxation calculations suggest that the structural relaxation around the transition metal impurities is quite local and mainly concern the coordination shell. This point is confirmed by the calculations of

the atomic displacements between the *relaxed* and *non-relaxed*. Fig. 4 represents the norm $|\vec{V}_i|$ as a function of the distance between the impurity and its neighbors in the *relaxed* model. It clearly shows that the oxygen coordination shell absorbs almost the relaxation. The displacement of atoms farther than 2.5\AA from the impurity is less than 0.035\AA . Comparing the three compounds, one also observes that the relaxation is slightly larger around titanium and iron than around chromium.

B. Core-hole effects

The influence of the core-hole can be described by calculating a self-consistent potential around a core-hole or by solving a Bethe-Salpeter equation.^{40,41} For impurity systems, solving a Bethe-Salpeter equation is probably beyond the reach of available computer programs. Moreover, it was already observed that both methods give quite similar results.⁵ Therefore, we shall describe the influence of the core-hole by calculating a self-consistent potential in the presence of a $1s$ core-hole.

Calculated spectra performed with or without the presence of a $1s$ core-hole on the chromium absorbing atom are compared in Fig. 5. It clearly appears that the core-hole is needed to obtain a good agreement with the experimental curve. In particular, the intensity and the energy positions of the features within the $6005\text{--}6017\text{ eV}$ energy range are not well reproduced if the core-hole is not taken into account in the calculation. We have noticed similar behaviors due to the presence of the core-hole at the titanium and iron K -edges in $\alpha\text{-Al}_2\text{O}_3\text{:Ti}^{3+}$ and $\alpha\text{-Al}_2\text{O}_3\text{:Fe}^{3+}$, respectively.

On the other hand, the presence of the core-hole has a non-negligible impact in the pre-edge region. This is illustrated in the inset of Fig. 5, which represents the pre-edge region ($5985\text{--}5998\text{ eV}$) of the Cr K edge in $\alpha\text{-Al}_2\text{O}_3\text{:Cr}^{3+}$. An interpretation of this region in terms of group theory has been detailed in Ref.⁴² In the pre-edge region both electric dipole ($1s \rightarrow p$) and quadrupole ($1s \rightarrow 3d$) transitions occur. Since the site of the impurity in doped $\alpha\text{-Al}_2\text{O}_3$ is not centrosymmetric, the p states are present in the pre-edge through $p-d$ hybridization. electric dipole ($1s \rightarrow p$) and quadrupole ($1s \rightarrow 3d$) transitions occur. Since the site of the impurity in doped $\alpha\text{-Al}_2\text{O}_3$ is not centrosymmetric, the p states are present in the pre-edge through $p-d$ hybridization. The calculated curves shown in the inset of Fig. 5 are the sum of both contributions. For the calculation of electric quadrupole transitions, the direction of the wave vector of the photon beam, \mathbf{k} , has to be specified. In the experiments, the single crystals were placed on the rotating holder so that the wave vector was parallel to the $[10\bar{1}]$ crystallographic direction. Consequently, the spectra $(\sigma_{\parallel} + 2\sigma_{\perp})/3$ shown in Fig. 5 are calculated with $\mathbf{k} // [10\bar{1}]$.⁴³ The two features of the experimental pre-edge are reproduced with or without the $1s$ core-hole (see inset of Fig. 5). The presence of the core-hole essentially provokes a 2.5 eV shift towards lower en-

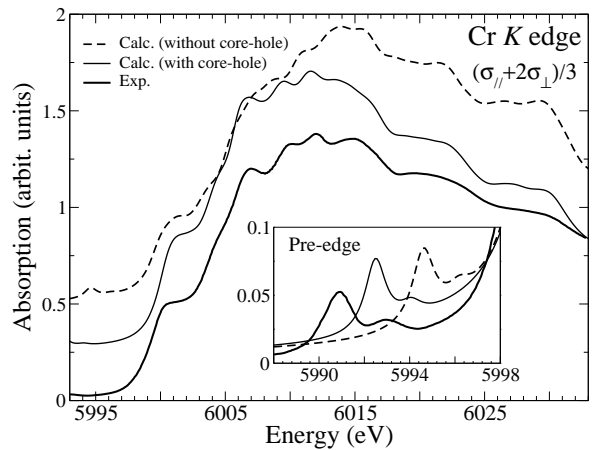


FIG. 5: Influence of the core-hole effects in XANES calculation at the Cr K edge in ruby. Inset: zoom of the pre-edge region. For pre-edge simulations, the calculated spectra include both electric dipole and electric quadrupole transitions (the wave vector \mathbf{k} is along the $[10\bar{1}]$ direction of the trigonal cell of ruby⁴³).

ergy of the pre-edge features, while the main rising edge is not shifted. A similar energy shift due to the core-hole was already observed for electric quadrupole transitions at the Ti K pre-edge in rutile.⁴⁴ Unfortunately, here the shift induced by the presence of the core-hole is not large enough to give a perfect agreement with experiment. This problem may be due to the limit of the density functional theory within LDA to model the core-hole-electron interaction for empty d states of $3d$ transition metals. LDA+U calculations could possibly improve the agreement in the pre-edge region. Indeed in Ref.⁴⁵, the authors show that LDA+U calculations performed on ruby essentially affect the positions of Cr d level relative to the valence and the conduction band.

C. Comparison between experimental and calculated XANES spectra

Fig. 6 compares experimental XANES data with the theoretical spectra obtained with the *relaxed* models. The $(\sigma_{\parallel} + 2\sigma_{\perp})/3$ and $\sigma_{\parallel} - \sigma_{\perp}$ signals are displayed at the Ti K edge for the pink sapphire sample (Fig.6a), at the Cr K edge for the ruby sample (Fig.6b) and at the Fe K edge for the blue sapphire sample (Fig.6c).

One observes that the experimental spectra present comparable overall shapes. The Fe K edge seems to be less resolved than the Ti and Cr K edges, probably due to the following two reasons: (i) the core-hole lifetime is shorter at the Fe K -edge (1.25 eV) than at the Cr K -edge (1.08 eV) and at the Ti K -edge (0.94 eV);³¹ (ii) the instrumental resolution is estimated to 0.9 eV at the Fe K -edge while it is $0.6\text{--}0.7\text{ eV}$ at both the Cr and Ti K -edges. We also noticed similarities between the M K edges (M=Ti, Cr, Fe) in $\alpha\text{-Al}_2\text{O}_3\text{:M}^{3+}$ and in $\alpha\text{-M}_2\text{O}_3$

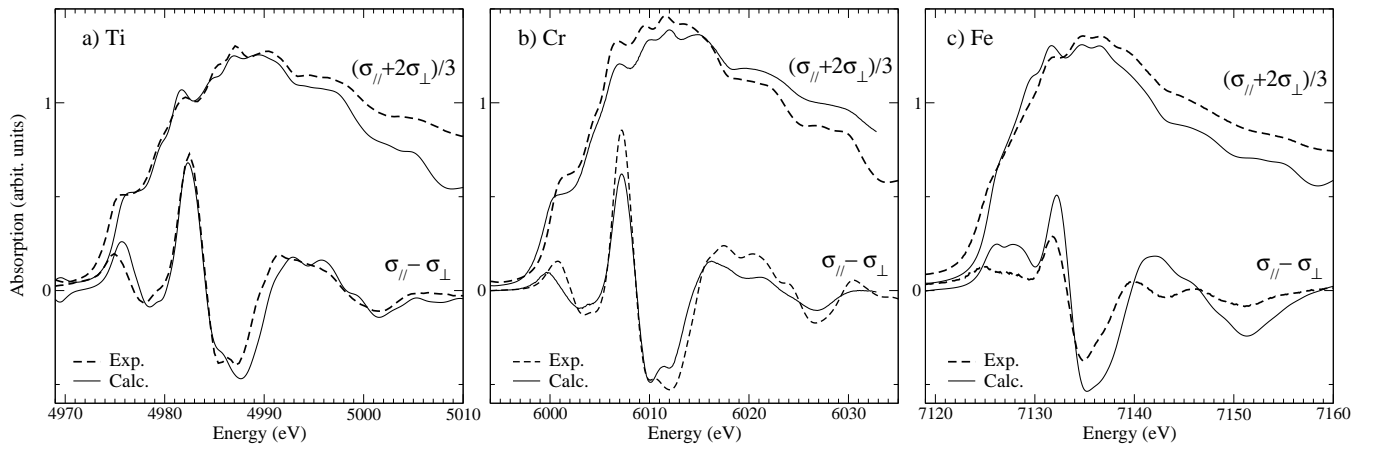


FIG. 6: Comparison between experimental XANES data (dashed line) and calculated spectra obtained with the *relaxed* models (solid line): a) the Ti *K* edge in pink sapphire ($\alpha\text{-Al}_2\text{O}_3\text{:Ti}^{3+}$); b) the Cr *K* edge in ruby ($\alpha\text{-Al}_2\text{O}_3\text{:Cr}^{3+}$); c) the Fe *K* edge in blue sapphire ($\alpha\text{-Al}_2\text{O}_3\text{:Fe-Ti}$). An energy shift was added to valence band maximum in the calculations in order to match with experiments: 4966 eV at the Ti *K* edge, 5991 eV at the Cr *K* edge and 7118 eV at the Fe *K* edge.

(see Ref.⁴⁶ for the Cr K edge in α -Cr₂O₃ and the Fe K edge in α -Fe₂O₃, and Ref.⁴⁷ for the Ti K edge in α -Ti₂O₃). At least to a certain extent, these spectra could be considered as the signature of a transition metal ion with a +III oxydation state in six-fold coordinated environment. However it is here necessary to perform calculations to go farther in the XANES analysis.

It can be seen in Fig. 6 that a good agreement is obtained between experimental data and calculated spectra carried out on the *relaxed* structural models. The agreement is especially good for ruby at the Cr K edge, where energy positions and relative intensities of the various features are well reproduced. It should be emphasized that not only the averaged $(\sigma_{\parallel} + 2\sigma_{\perp})/3$ spectra are correctly reproduced, but also the dichroic signal, from which more precise structural information could be extracted. Such a good agreement with angular dependent spectra has been also obtained with the same calculation method: at the Al K edge in corundum²¹ and at the Si K edge in α -quartz.⁵

We have seen in Sec. III A that the differences between the *relaxed* and *non-relaxed* structures are essentially concerned with the interatomic distances within the coordination shell of the impurity. Therefore, it is interesting to test the sensitivity of XANES to such subtle structural modifications. Fig. 7 compares σ_{\parallel} and σ_{\perp} experimental spectra with the corresponding calculated ones performed from both *non-relaxed* and *relaxed* models. First of all, it is worth noting that the differences observed between calculated spectra are small but not negligible. For all compounds, peaks labeled g in σ_{\parallel} and labeled I and J in σ_{\perp} are too strong in the *non-relaxed* calculated spectra. Consequently, these features (all located at about 30 eV above the edge) are clearly correlated to the first interatomic distances around the impurity. The same conclusion can be made for the shoulders labeled A and B in σ_{\perp} and b in σ_{\parallel} . Especially at the Cr K edge in σ_{\perp} signal, one can see that the double-feature (D and E) is better reproduced by the *relaxed* calculation than by the *non-relaxed* one.

In a previous study,³ the *relaxed* model was validated up to the second neighbors around the impurity by comparison with EXAFS measurements. Here, thanks to the very good agreement obtained between experimental and *relaxed* calculated XANES spectra, the *relaxed* structural model is again validated and this time to greater extent.

IV. CONCLUSIONS

In this paper, we have shown that XANES can provide precious information about the small structural relaxation occurring within the atomic site of impurity in an aluminum oxide matrix. This has been achieved by (i) measuring angular dependent XANES spectra in order to probe the distortion of the impurity site, (ii) calculating structural model by ab initio energy minimization, (iii) calculating the XANES spectra from the previ-

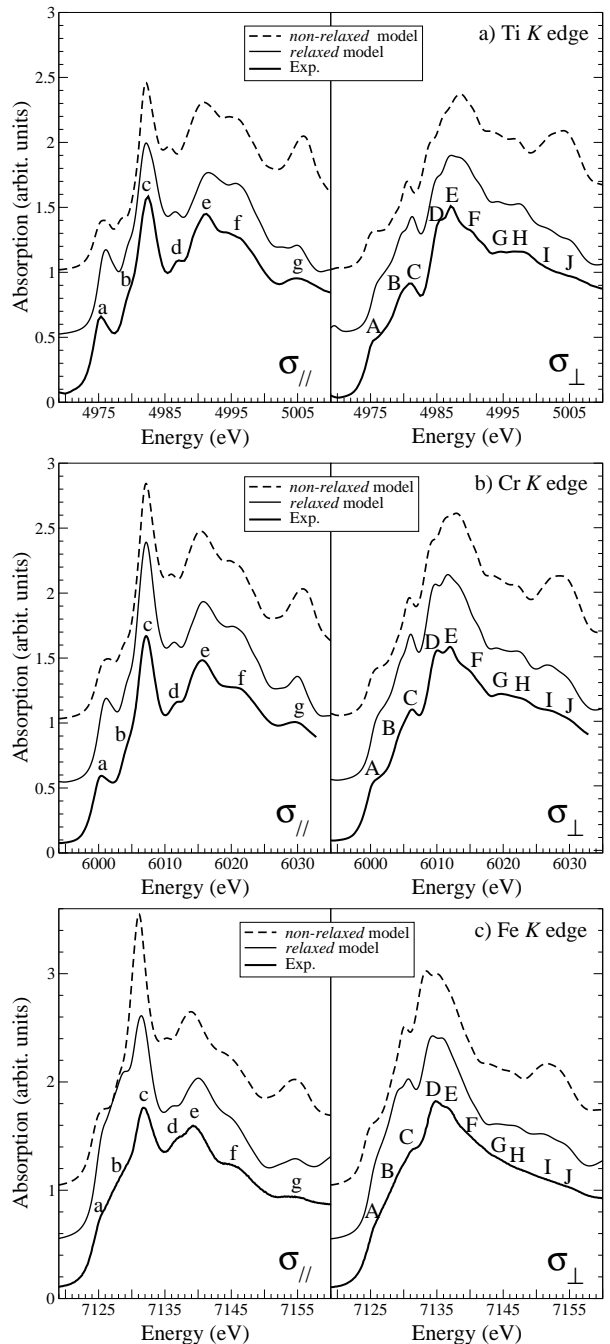


FIG. 7: Comparison between σ_{\parallel} (left) and σ_{\perp} (right) experimental data (thick solid line) and calculated spectra obtained with both *relaxed* model (thin solid line) and *non-relaxed* model (dashed line): a) the Ti K edge in pink sapphire, α -Al₂O₃:Ti³⁺; b) the Cr K edge in ruby, α -Al₂O₃:Cr³⁺; c) the Fe K edge in blue sapphire, α -Al₂O₃:Fe-Ti.

ous theoretical structural models using the full-potential pseudopotential self-consistent method of Ref.⁵ The good agreement obtained between experimental and calculated spectra permits the validation of the structural models. We have also pointed out the importance of the electronic potential construction to carry this study to a suc-

cessful conclusion. These results opens new applications in XANES analysis, in particular for dilute samples for which good quality EXAFS measurements are difficult to collect.

Acknowledgments

We wish to acknowledge the computational support of the French *Institut du Développement et de Recherche en*

Informatique Scientifique in Orsay, where all the calculations of this study were carried out.

-
- ¹ H. Miller, *Physica C* **104**, 183 (1981).
- ² J. D. Verhoeven, A. H. Pendray, and W. E. Dauksch, *JOM* **50**, 58 (1998).
- ³ E. Gaudry, A. Kiratisin, Ph. Sainctavit, Ch. Brouder, F. Mauri, A. Ramos, A. Rogalev, and J. Goulon, *Phys. Rev. B* **67**, 094108:1 (2003).
- ⁴ G. A. Waychunas, C. C. Fuller, J. A. Davis, and J. J. Rehr, *Geochim. Cosmochim. Acta* **67**, 1031 (2003).
- ⁵ M. Taillefumier, D. Cabaret, A.-M. Flank, and F. Mauri, *Phys. Rev. B* **66**, 195107 (2002).
- ⁶ R. G. Burns, *Mineralogical Applications of Cristal Field Theory*, vol. 5 of *Cambridge topics in Mineral Physics and Chemistry* (Cambridge University Press, 1993), 2nd ed.
- ⁷ K. Nassau, *The Physics and Chemistry of Color* (Wiley Interscience, 1983).
- ⁸ R. Newnham and Y. de Haan, *Zeit. Kristallogr.* **117**, 235 (1962).
- ⁹ H. K. Eigenmann, Ph.D. thesis, Eidgenössischen Technischen Hochschule, Zürich (1970).
- ¹⁰ J. Goulon, A. Rogalev, C. Gauthier, C. Goulon-Ginet, S. Paste, R. Signorato, C. Neumann, L. Varga, and C. Malgrange, *J. Synchrotron Rad.* **5**, 232 (1998).
- ¹¹ A. Rogalev, J. Goulon, C. Goulon-Ginet, and C. Malgrange, in *Magnetism and Synchrotron Radiation*, edited by E. Beaurepaire, F. Scheurer, G. Krill, and J.-P. Kappler (Springer, 2001).
- ¹² R. Car and M. Parrinello, *Phys. Rev. Lett.* **55**, 2471 (1985).
- ¹³ "CPMD V3.7 Copyright IBM Corp 1990-2003, Copyright MPI fuer Festkoerperforschung Stuttgart 1997-2001". For more information see <http://www.cpmc.org>.
- ¹⁴ Calculations were performed with PARATEC (PARAllel Total Energy Code) by B. Pfrommer, D. Raczkowski, A. Canning, S.G. Louie, Lawrence Berkeley National Laboratory (with contributions from F. Mauri, M. Cote, Y. Yoon, Ch. Pickard and P. Haynes). For more information see www.nersc.gov/projects/paratec.
- ¹⁵ N. Troullier and J. L. Martins, *Phys. Rev. B* **43**, 1993 (1991).
- ¹⁶ L. Kleinman and D. M. Bylander, *Phys. Rev. Lett.* **48**, 1425 (1982).
- ¹⁷ W. Duan, R. M. Wentzcovitch, and K. T. Thomson, *Phys. Rev. B* **57**, 10363:10369 (1998).
- ¹⁸ W. Duan, G. Paiva, R. M. Wentzcovitch, and A. Fazzio, *Phys. Rev. Lett.* **81**, 3267 (1998).
- ¹⁹ Within the $R\bar{3}c$ space group, the 4 c symmetry site corresponds to the positions $\pm(x, x, x; x + \frac{1}{2}, x + \frac{1}{2}, x + \frac{1}{2})$ and the 6 e symmetry site corresponds to the positions $\pm(x, \frac{1}{2} - x, \frac{1}{4}; \frac{1}{2} - x, \frac{1}{4}, x; \frac{1}{4}, x, \frac{1}{2} - x)$.
- ²⁰ A. Lever, *Inorganic Electronic Spectroscopy* (Elsevier, 1984).
- ²¹ D. Cabaret, E. Gaudry, M. Taillefumier, P. Sainctavit, and F. Mauri, *Physica Scripta*, Proc. XAFS-12 conference (2004), to be published.
- ²² P. E. Blöchl, *Phys. Rev. B* **50**, 17953 (1994).
- ²³ R. Haydock, V. Heine, and M. J. Kelly, *J. Phys. C: Solid State Phys.* **5**, 2845 (1972).
- ²⁴ R. Haydock, V. Heine, and M. J. Kelly, *J. Phys. C: Solid State Phys.* **8**, 2591 (1975).
- ²⁵ For electric dipole and quadrupole transitions, the operator \mathcal{D} of Eq.2 in Ref.⁵ is equal to $\hat{\epsilon} \cdot \mathbf{r}$ and to $\frac{i}{2} \hat{\epsilon} \cdot \mathbf{r} \mathbf{k} \cdot \mathbf{r}$, respectively. The unit vector $\hat{\epsilon}$ is the direction of the polarisation of the incident photon beam, and \mathbf{k} is the wave vector.
- ²⁶ A. L. Ankudinov, B. Ravel, J. J. Rehr, and S. D. Conradson, *Phys. Rev. B* **58**, 7565 (1998).
- ²⁷ C. R. Natoli, D. K. Misemer, S. Doniach, and F. W. Kutzler, *Phys. Rev. A* **22**, 1104 (1980).
- ²⁸ M. Benfatto, S. D. Longa, and C. R. Natoli, *J. Synchrotron Rad.* **10**, 51 (2003).
- ²⁹ H. J. Monkhorst and J. D. Pack, *Phys. Rev. B* **13**, 5188 (1976).
- ³⁰ J. Kokubun, K. Ishida, D. Cabaret, F. Mauri, R. V. Vedrinskii, V. L. Kraizman, A. A. Novakovich, E. V. Krivitskii, and V. E. Dmitrienko, *Phys. Rev. B* **69**, 245103 (2004).
- ³¹ M. Krause and J. Oliver, *J. Phys. Chem. Ref. Data* **8**, 329 (1979).
- ³² N. Laurance, E. C. McIrvine, and J. Lambe, *J. Phys. Chem. Solids* **23**, 515 (1962).
- ³³ L. L. Lohr and W. H. Lipscomb, *J. Chem. Phys.* **38**, 1607 (1963).
- ³⁴ S. C. Moss and R. E. Newnham, *Zeitschr. Kristallogr.* **120**, 359 (1964).
- ³⁵ J. W. McCauley and G. V. Gibbs, *Zeitschr. Kristallogr.* **135**, 453 (1972).
- ³⁶ P. Kizler, J. He, D. R. Clarke, and P. R. Kenway, *J. Am. Ceram. Soc.* **79**, 3 (1996).
- ³⁷ W.-C. Zheng, *Physica B* **245**, 119 (1998).
- ³⁸ R. D. Shannon, *Acta. Cryst.* **A32**, 751 (1976).
- ³⁹ K. Langer, *Z. Kristallogr.* **216**, 87 (2001).
- ⁴⁰ E. L. Shirley, *Phys. Rev. Lett.* **80**, 794 (1998).
- ⁴¹ J. A. Soininen and E. L. Shirley, *Phys. Rev. B* **64**, 165112(1) (2001).
- ⁴² E. Gaudry, D. Cabaret, Ph. Sainctavit, Ch. Brouder, F. Mauri, A. Rogalev, and J. Goulon, *Physica Scripta Proc. XAFS-12, Sweden, 2003* (2004).

- ⁴³ One should keep in mind that $(\sigma_{\parallel} + 2\sigma_{\perp})/3$ is what has been measured. It corresponds to the isotropic spectrum only in the electric dipole approximation, but under no circumstances in the electric quadrupole approximation.
- ⁴⁴ Y. Joly, D. Cabaret, H. Renevier, and C. R. Natoli, *Phys. Rev. Lett.* **82**, 2398 (1999).
- ⁴⁵ V. V. Mazurenko, A. N. Varaksin, V. G. Mazurenko, V. S. Kortov, and V. I. Anisimov, *Physica B* **344**, 385 (2004).
- ⁴⁶ L. A. Grunes, *Phys. Rev. B* **27**, 2111 (1983).
- ⁴⁷ G. A. Waychunas, *Am. Mineral.* **72**, 89 (1987).
- ⁴⁸ L. W. Finger and R. M. Hazen, *J. Appl. Phys.* **51** (1980).